Ferrihydrite formation: the role of Fe_{13} Keggin clusters

*Joshua S. Weatherill[a], Katherine Morris[a], Pieter Bots[a†], Tomasz M. Stawski[b,c], Arne Janssen[d], Liam Abrahamsen[e], Richard Blackham[f] and Samuel Shaw[a]**

[a]Williamson Research Centre, School of Earth and Environmental Science, University of Manchester, Oxford Road, Manchester, M13 9PL, UK. [b]School of Earth and Environment, University of Leeds, Leeds, LS2 9JT, UK. [c]German Research Centre for Geosciences, GFZ, 14473, Potsdam, Germany. [d]School of Materials, University of Manchester, Oxford Road, Manchester, M13 9PL, UK. [e]National Nuclear Laboratory, Chadwick House, Warrington Road, Birchwood Park, Warrington, WA3 6AE, UK. [f]Sellafield Ltd, Hinton House, Birchwood Park Avenue, Risley, Warrington, Cheshire, WA3 6GR, UK

ABSTRACT

Ferrihydrite is the most common iron oxyhydroxide found in soil and is a key sequester of contaminants in the environment. Ferrihydrite formation is also a common component of many treatment processes for clean-up of industrial effluents. Here we characterize ferrihydrite formation during the titration of an acidic ferric nitrate solution with NaOH. In-situ SAXS measurements supported by ex situ TEM indicate that initailly Fe_{13} Keggin clusters (radius ~0.45 nm) form in solution at pH 0.5 - 1.5, and are persistant for at least 18 days. The Fe_{13} clusters

begin to aggregate above ~ pH 1, initially forming highly linear structures. Above pH ~ 2 densification of the aggregates occurs in conjunction with precipiation of low molecular weight Fe(III) speices (e.g. monomers, dimers) to form mass fractal aggregates of ferrihydrite nanoparticles (~ 3 nm) in which the Fe_{13} Keggin motif is preserved. SAXS analysis indicates the ferrihydrite particles have a core-shell structure consisting of a Keggin center surrounded by a Fe-depleted shell, supporting the surface depleted model of ferrihydrite. Overall, we present the first direct evidence for the role of Fe_{13} clusters in the pathway of ferrihydrite formation during base hydrolysis, showing clear structural continuity from isolated Fe_{13} Keggins to the ferrihydrite particle structure. The results have direct relevance to the fundamental understanding of ferrihydrite formation in environmental, engineered and industrial processes.

Introduction

Ferrihydrite is a nanoparticulate iron oxyhydroxide which is ubiquitous in the natural near-surface environment. It is also present in the core of the protein ferritin and has numerous industrial applications[1]. Due to its high adsorptive capacity and ability to co-precipitate aqueous ions, ferrihydrite is a crucial sequester of contaminants in both natural[2–4] and industrial systems[5]. The properties of ferrihydrite which control its reactivity are sensitive to the aqueous conditions and mechanisms of formation[6,7], therefore it is critical to have an understanding of ferrihydrite formation processes from solution at the molecular scale to underpin its environmental behavior and technological applications.

Ferrihydrite is the first product of induced ferric hydrolysis, and the phase that typically initially forms in natural aqueous environments[1]. Hydrolysis of ferric iron and subsequent precipitation of ferrihydrite from solution has been studied extensively[e.g.8–13]. The classic model indicates formation proceeds by successive polymerization steps: solvated Fe(III) ions undergo hydrolysis to form low molecular weight hydrated Fe(III) species (dimers, trimers), which go on to interact via olation and oxolation to form ferric species of higher nuclearity, leading to nucleation (i.e. formation) of ferrihydrite nanoparticles from solution. However, details of the ferric hydrolysis mechanisms are complex, and the extensive literature does not provide a unified view of ferrihydrite formation. Due to the high charge density of Fe(III), the hydrolysis reactions occur rapidly, rendering the isolation and characterization of intermediate hydrolysis products challenging. As such, the pathways from monomer to ferrihydrite and the structure of any intermediate species are unclear.

Recent studies have indicated that the μ-oxo Fe(III) dimer is the dominant species in partially-hydrolyzed ferric solutions[14–16], with no larger Fe(III) oligomers detected. Other studies have similarly concluded that no polycations larger than the Fe(III) dimer are detectable[17], whilst some have reported formation of an Fe(III) trimer[18,19], tetramer[20] and larger polycations[21]. However, there is little consistency on the composition of the larger Fe(III) polymers, and some of them may already be considered a ferrihydrite phase[15].

Larger metal polycations have been identified in other hydrolysable trivalent element systems such as Cr(III)[22,23], Ga(III)[24,25] and Al(III)[26–28]. The most studied of these polycations is the Al_{13} Keggin, consisting of a central tetrahedral Al unit surrounded by octahedral Al units[29]. Al_{13} is an important intermediate in the pathway from Al monomers to solid Al hydroxides[28,30]. Due to similar aqueous chemistries of Fe(III) and Al(III), it has been postulated that an analogous Fe_{13}

63 Keggin cluster may exist[25]. Indeed, recently Sadeghi *et al.*[31] successfully synthesised and
64 characterised a Fe_{13} Keggin cluster using stabilisation with Bi^{3+} ions. Although the details of the
65 ferrihydrite structure remain unclear, the single phase model proposed by Michel *et al.*[32] and
66 subsequently adopted in the wider literature[33–36] is based on linked Keggin units. This raises the
67 question of whether Fe_{13} is a precursor (i.e. prenucleation cluster[37]) to ferrihydrite formation, but
68 as yet, a pathway from monomers to Fe_{13} and then ferrihydrite during base hydrolysis has yet to
69 be demonstrated.

70 After the nucleation and growth of individual ferrihydrite nanoparticles aggregation may
71 occur, even several pH units away from the point of zero charge (PZC)[38]. Aggregates of
72 ferrihydrite nanoparticles can possess low mass fractal dimensions (< 1.1), enabling formation of
73 large (μm scale), low-density structures that exist as stable colloidal suspensions[39,40]. These
74 structures may undergo collapse to form denser, settleable aggregates upon a change in solution
75 conditions, such as increased ionic strength[40]. These nanoparticle aggregation processes are
76 important because the resulting ferrihydrite aggregate structure impacts colloidal stability[39,41],
77 reactivity[42–44], transport behaviour[40] and also filterability in wastewater treatment processes[45].

78 In order to observe intermediate species during rapid Fe(III) hydrolysis, the majority of
79 experiments to date have been conducted in quasi-equilibrated solution at constant pH or a given
80 OH/Fe ratio[46]. The conclusions from these studies will have limited relevance to ferrihydrite
81 formation in dynamic processes relevant to effluent treatment and environmental systems. The
82 Enhanced Actinide Removal Plant (EARP)[47,48] (Sellafield, UK) is an example of an effluent
83 treatment processes where this is relevant. Here, a ferric oxyhydroxide floc formed via base
84 hydrolysis is used to treat highly radioactive effluents generated from the reprocessing of spent
85 nuclear fuel[47,48]. During the EARP process, radionuclides become associated with the floc which

is subsequently separated by ultrafiltration and encapsulated in a cement wasteform. The EARP effluent compositions are expected to significantly change when the site transitions from reprocessing to post-operational clean-out and decommissioning activities over the next few years. Therefore, to enable better control of the EARP process and similar industrial treatments, an enhanced understanding of the ferrihydrite formation mechanisms under process relevant conditions is essential, and provides fundamental knowledge relating to ferrihydrite formation.

In this study we determine the mechanisms by which ferrihydrite nanoparticles form, and the role of Fe_{13} clusters, during the controlled hydrolysis of an acidic ferric nitrate solution in an experimental protocol designed to mimic ferric oxyhydroxide effluent treatment systems (e.g. EARP). To achieve this, *in situ* time-resolved small angle X-ray scattering (SAXS) experiments followed ferrihydrite formation. These were augmented with *ex-situ* X-ray diffraction (XRD) and transmission electron microscopy (TEM) techniques. Results show that during base hydrolysis, ferrihydrite nanoparticles form via Fe_{13} Keggin clusters. This is key to understanding the pathway of ferrihydrite formation in environmental, engineered and industrial processes.

Experimental Methods

Ferrihydrite was synthesized in an automated computer-controlled reactor (Applikon MiniBio) with temperature control (Peltier heater/ cooler) via NaOH-induced hydrolysis of ferric nitrate solutions. Stirred batch experiments were conducted at 35 °C (representative of EARP conditions), with the pH and temperature monitored throughout. Starting solutions consisted of 400 ml of $Fe(NO_3)_3.9H_2O$ in 1 M HNO_3 (7.16 mM Fe(III)). In the standard base addition experiments 7 M NaOH was initially added at a rate of 1.5 ml min^{-1} until pH 2.3, then 0.3 ml

min^{-1} until pH 3 and finally, after pH 3, 0.2 M NaOH was added at 1.5 ml min^{-1} to pH 9 (Video S1). To test the effect of the NaOH addition rate, further slow NaOH addition experiments were performed with 7 M NaOH additions at 0.3 ml min^{-1} up to pH 1.2. To provide an indication of the reaction progress, Figure S10 shows change in pH with time in both standard and slow addition experiments. Solid products were isolated by centrifuging and washing three times with deionized water before drying at 40°C overnight. Powder XRD (Bruker D8 Advance), BET surface area analysis (Micromeritics Gemini) and TEM images of the dried products were obtained (SI).

During the standard NaOH addition experiment (1.5 ml min^{-1}), dissolved iron concentrations were determined following filtration (0.22 μm polyethersulfone) then analysis for Fe using the ferrozine method[49]. A separate experiment using ultrafilters (10 and 3 kDa) was also undertaken on selected samples (SI).

To enable comparison with iron behavior at thermodynamic equilibrium, the ferrihydrite synthesis procedure was modelled in PHREEQC[50] by mimicking the NaOH-induced hydrolysis of $Fe(NO_3)_3$ undertaken in the experimental method (SI).

Time-resolved *in situ* SAXS experiments. Ferrihydrite synthesis experiments were performed *in situ* on beamline I22 at the Diamond Light Source with time-resolved SAXS data collected throughout base addition. A peristaltic pump in closed loop configuration continuously circulated the reacting suspension from the continuously stirred reaction vessel through a quartz capillary in-line with the X-ray beam[51]. Flow time betweeen the reaction vessel and the quartz capillary was kept short (< 2 s). A monochromatic X-ray beam at 12.4 KeV and a camera length of 3.8 m was used in the time resolved experiments, and the SAXS patterns were collected using

a pixel-array PILATUS 2M detector. SAXS patterns were collected throughout the reaction and for 30 min after base addition had finished, with a time resolution of 15 seconds/frame.

SAXS experiments were also undertaken on aged, static samples. For these samples, the ferrihydrite synthesis reaction was stopped at pH 0.5 or pH 1.5, and the resulting solutions aged at 35 °C for 6 and 18 days prior to SAXS analysis. Here, samples were directly injected into a quartz capillary and SAXS data were collected using a camera length of 1.9 m.

SAXS data analysis. The scattering curves were fit using a model that describes the scattering as arising from a population of spherical primary particles which may cluster to form aggregates with both mass fractal-like structure (mass fractal structure factor) and non-fractal aggregates (hard sphere structure factor)[52] (SI).

Results and Discussion

Solid phase characterization and solution analysis. XRD characterization (Figure S1) of solid product isolated at pH 9 indicate that two-line ferrihydrite[53] was the reaction product formed with a BET surface area of 290 ± 15 m^2 g^{-1}. TEM on samples collected at pH 1, 3 and 9 (Figure 4 and S13) show that the composition, stucture and morphology of the particles were consistant with 2-line ferrihydrite, with no other phases detected.

In the standard base addition experiment, the "dissolved Fe" (< 0.22 μm, $Fe(III)_{aq}$) concentration decreased slightly (~ 5%) between pH 0.1 and 1, followed by a more significant decrease after pH 1 (Figure 1 & S3). The experimental pH at which $Fe(III)_{aq}$ removal occured (> pH 0.1) was lower than that predicted by thermodynamic calculation, which indicated $Fe(III)_{aq}$ would be constant until pH 2.5 (Figure 1). The thermodynamic calculations are based on the

principles of classical nucleation theory (CNT), and as such $Fe(III)_{aq}$ is predicted to remain constant until the solution becomes saturated with respect to ferrihydrite ($Fe(OH)_3$), at which point instantaneous precipitation is predicted to occur. However, it should be noted that filtration analysis and thermodynamic modelling can not determine the presence of large Fe(III) polycations (e.g. Keggins) which may be present within the partially hydrolysed solution. The experimental data instead showed an ~ 35% decrease in $Fe(III)_{aq}$ below pH 2.5. Above pH 2.5 experimental data showed a rapid decease in $Fe(III)_{aq}$ consistent with the thermodynamic predictions for ferrihydrite formation. Above pH 4 there was no detectable $Fe(III)_{aq}$ in solution (< 0.01 ppm), indicating ferrihydrite formation was complete. A separate experiment, performed under identical experimental conditions but with the additional use of ultrafilters, showed a similar result and is detailed in SI (Figure S3).

The discrepancy between the experimental and theoretical results reflects the dynamic nature of our experiments. PHREEQC calculations allow thermodynamic equilibrium to be achieved upon each small addition of base, whilst experimentally, constant base addition means equilibrium is not achieved. Locally high pH at the point of base addition, indicated by bursts of yellow/orange color in the experimental system (Video S1), likely drives Fe(III) cluster/particle formation at lower pH, and therefore may explain the discrepancy with the theoretical results. Interestingly, analysis of aged solutions (Figure S2) indicates that the $Fe(III)_{aq}$ concentration in pH 1.5 solution remained suppressed after 7 days aging, suggesting the Fe(III) clusters/particles present are thermodynamically (meta)stable. This was noteworthy considering that ferrihydrite is significantly undersaturated (saturation index ~ -2.7) at pH 1.5 (Figure 1) and suggests irreversible formation of Fe(III) clusters/particles is occurring during base addition in this system.

Overview of SAXS data. Figure 2A and S4 shows the evolution in the SAXS patterns during the standard NaOH addition experiment as the pH increases. Below pH 0.12 the scattering patterns had no intensity above background confirming that there were no scattering species present, and therefore Fe(III) was present only as monomers (Figure S5). Above pH 0.12, increased scattering intensity occurred indicating the formation of clusters/particles and allowing fitting of the scattering patterns. Between pH 0.12 and 1, fits were obtained using a single population of clusters/particles, whilst above pH 1 fits required the addition of the mass fractal / hard sphere structure factor in order to accommodate the increased scattering intensity seen in the low-q region (Eq S2, S3). From this, and in conjunction with other data discussed below, two characteristic stages of ferrihydrite formation were identified:

Stage (i): pH 0.12 to ~ 1: formation of primary Fe_{13} Keggin clusters.

Stage (ii): pH ~ 1 to 9: formation and aggregatation of 2-line ferrihydrite nanopartles.

Stage (i): formation of primary Fe_{13} Keggin clusters. Log-log plots of the SAXS patterns (Figure 2A and S4) showed a visible Guinier region in the high-q area ($q > 1$ nm^{-1}) at pH 0.15 indicating the presence of a single population of unaggregated clusters[54]. These initiated at pH 0.12 and within 2 mins of starting the NaOH addition (Figure S5). From pH 0.12 – 1, the clusters grew in number density (n, Eq S2) whilst being relatively stable in size, as evidenced by an increasing scattering intensity (I(q)) throughout the q-range without any change in the overall SAXS pattern shape (Figure 2A). The growing number of clusters can also be seen by the increasing value of the pre-factor term $nV_p^2\Delta\rho^2$ up to pH 1 (Figure 2B). Fits to the scattering patterns below pH 1 were obtained for $q > 0.5$ nm^{-1} using a single cluster population with a spherical form factor (Eq S2). The fitted cluster radius (r_0) was initially 0.44 nm at pH 0.15 and decreased slightly to 0.41 nm by pH ~ 1 (Figure 2B), a decrease of 0.03 nm which is within the

inherent uncertainty of SAXS and may be due to slight changes in the background scattering[55]. Similarly, Guinier analysis[54] of the scattering patterns up to pH 1 gives a radius of gyration Rg (a shape independent measure of size) of 0.36 – 0.37 nm (Figure S6), corresponding to a spherical radius of 0.46 – 0.48 nm. Above pH ~ 1 Guinier analyses was not possible due to development of upward curvature in the low-q Guinier region of the SAXS pattern, indicating cluster aggregation. Overall, these results show strong agreement in the cluster radius and within the expected limitations imposed by background subtraction at high-q values, confirm a cluster of ~ 0.45 nm radius is forming at pH 0.12 – ~ 1.

Scattering patterns collected during the slow NaOH addition experiment (0.3 ml min^{-1} addition rate) show essentially the same results as described above (Figure S6 and S7). Therefore, formation of clusters was independent of addition rates in these experiments where base addition from pH 0.1 to 1 was between 32 min and 174 min in the standard and slow addition experiments, respectively.

By ~ pH 1.5 the uniform increase in scattering intensity across the entire q-range was complete; any additional scattering intensity increases were then concentrated in the low-q region and resulted from cluster/particle aggregation (discussed below). This confirms that primary cluster formation was complete by pH ~ 1.5 and is supported by the pre-factor $nV_p^2\Delta\rho^2$ reaching a maximum value by pH ~ 1.5 (Figure 2B).

Formation of these (meta)stable clusters at low pH values was not predicted. Based on thermodynamic modelling[56] and previous studies[9,57–59], it was expected that iron would be present as unfilterable monomers and small hydrolysis products (dimers, ~ 0.33 nm spherical radius[60]) below pH 1 which are too small to be the ~ 0.45 nm radius clusters we observed (Figure S11)[60]. The sub-nm size of the primary clusters indicates that they are best described as clusters

of ions rather than a phase with extended structure such as a ferrihydrite particle. Additionally, their size is significantly smaller than reported ferrihydrite particle radii of 0.8 – 5 nm[1,61,62]. For these reasons it appears that the primary clusters are most likely precursors to ferrihydrite formation rather than already formed ferrihydrite particles. Sadeghi *et al.* (2015)[31] recently synthesized and isolated a Fe_{13} oxo-iron cluster with the α-Keggin structure. Because the ferrihydrite structure in the Michel *et al.* model[32] is considered to be linked Fe_{13} Keggin units, this Fe_{13} cluster has been identified as a potential prenucleation cluster to ferrihydrite formation. This is analogous to the Al_{13} cluster being a precursor to aluminum hydroxide formation[28]. The Fe_{13} cluster has an R_g of 0.36 - 0.38 nm (ref 31 and Figure 3), corresponding to a spherical radius of 0.46 - 0.49 nm. This closely matches the cluster size measured in the current study with a Guinier radius of gyration of 0.36 nm and a corresponding spherical cluster radius of 0.46 nm. In addition, an excellent match is observed between simulated scattering from Fe_{13} Keggin clusters[31] (using Crysol (SI)) and the measured scattering patterns (Figure 3). In contrast, simulated scattering patterns of the Fe oxo-dimer described by Zhu *et al.*[14,15] and an Fe trimer do not match to the experimental data and their R_g's are significantly smaller (0.24 – 0.26 nm, Figure S11). Taken as a whole, this indicates that Fe_{13} clusters form at low pH as a precursor / prenucleation cluster to ferrihydrite formation. However, it is likely that not all the Fe is present as Fe_{13} keggins, with a significant proportion likely to be monomers and smaller hydrolysis products (e..g dimer) which produce a minimal scattering contribution.

SAXS patterns collected on aged pH 0.5 samples (6 and 18 days at 35 °C) also show scattering indicative of a single population of clusters (Figure S8). Due to the use of a shorter camera length in these experiments, the q-range is shifted to higher values than in the main time-resolved experiments. Using Guinier analysis, the R_g of clusters in the pH 0.5 solutions (for 6 and 18

246 days) was 0.38 nm, identical to the Fe_{13} Keggin cluster[31]. Again, strong agreement is seen
247 between simulated Fe_{13} scattering patterns and the pH 0.5 aged samples (Figure S9). Therefore
248 the Fe_{13} clusters we observe forming in the dynamic experiments persist in solution for at least
249 18 days, consistent with the analogous Al_{13} cluster which is also persistent in solution[63–65].
250 Interestingly, the aged pH 1.5 samples also showed scattering indicative of a single population of
251 clusters (Figure S8). Since Fe_{13} clusters begin aggregating above ~ pH 1 in the main dynamic
252 experiment (see below), there may also be aggregates present at pH 1.5 which were unseen in the
253 experimental q-range. Alternatively, disaggregation over time may have occurred. The R_g of
254 clusters in the pH 1.5 solutions is 0.35 nm. This modest change in size from pH 0.5 may be an
255 artefact of small variation in the background solvent scattering as pH increases, or may reflect
256 slight changes to the shape / polydispersity of the primary clusters; Keggin clusters are not
257 perfect spheres and can assume different isomeric forms, as has been observed for Al_{13} clusters[29].
258 Additionally, lacunary Keggin structures with missing fragment(s) are known[66]. Nevertheless,
259 good agreement is seen between simulated Fe_{13} scattering patterns and the pH 1.5 aged samples
260 (Figure S9). Only a slight difference in the scattering intensity ($nV_p^2\Delta\rho^2$) was observed between
261 6 and 18 day samples at pH 0.5 and pH 1.5, suggesting there is no significant difference in the
262 number density of scattering particles (n, Eq S2) and thus no net formation or dissolution of
263 clusters between these time periods. Additionally, the pH of the solutions were essentially stable
264 during the ageing period (Table S2), indicating no further hydrolysis / condensation which would
265 release H^+[67].

266 TEM images obtained for the pH 1 sample (Figure 4A and S13A) showed loosely aggregated
267 nanoparticles that vary in size from ~ 2-5 nm diameter (Figure 4A). This aggregated phase could
268 be identified as 2-line ferrihydrite based on the lattice images and diffraction patterns observed

(Figure S13A). Solution data showed a small decrease (~5%) in $Fe(III)_{(aq)}$ by pH 1 (Figure 1), consistent with particle formation. The high angle annular dark field (HAADF) images provide additional evidence for smaller ~1-2 nm diameter aggregating units, putative evidence for Keggin clusters forming the particles (Figure 4A). Given the SAXS patterns at pH 1 are dominated by scattering from the Fe_{13} clusters, these data suggest that at this pH a small proportion of Fe_{13} clusters, and potentially other hydrolysis products, coalesce to form filterable ferrihydrite nanoparticles. However, TEM images likely over-represent the amount of ferrihydrite nanoparticles present in solution at pH 1, as the individual clusters themselves (as solution polycations) will not be observed via TEM.

Overall, these data confirm Fe_{13} Keggin clusters form rapidly upon NaOH addition and are stable in solution for weeks at low pH. With increasing pH ferrihydrite nanoparticles form and aggregation occurred.

Stage (ii): Formation and aggregatation of 2-line ferrihydrite nanopartles. Increasing scattering intensity in the low-q region of the SAXS patterns was observed above pH 1, indicating that aggregation of primary Fe_{13} clusters occured. Atom-by-atom growth of the clusters can be ruled out as no increase in the slope of Guinier region was observed (Figure S12). The low-q scattering intensity increase was fitted by introducing a mass fractal structure factor, permitting determination of the aggregate weighting factor (ε, smaller value = more aggregation), aggregate size parameter (ξ), and aggregate fractal dimension (d_f) (Eq S2). ε initially decreased slowly above pH 1 before decreasing rapidly from pH 2 – 3 and reaching a minimum at pH 4.1, indicating that aggregation is complete. This occurred concurrently with continual growth in the scattering intensity of the low-q region and confirms aggregation increases with increasing pH. This is consistent with solution data whereby the rapid decrease in

292 $Fe(III)_{aq}$ between pH 2 – 3 was concurrent with most rapid aggregate formation. Above pH 4.1, ε
293 shows a small increase until pH 5 and then stabilizes, presumably an artifact of the aggregate
294 size increasing to beyond the experimentally measured q-range . This can be seen in Kratky plots
295 ($I(q)*q^2$ vs. q, Figure S14B) where the low-q scattering intensity peak, indicative of average
296 aggregate size, moves to values outside the measured q-range above pH 4.1 and results in
297 reduced scattering intensity within the low-q area of the measured range.
298 Aggregation from as low as pH 1 is notable given that ferrihydrite has a PZC of ~ pH 8[1] and
299 may be due to a number of factors. Firstly, the high ionic strength [40,42,44] of our experiments, as
300 coagulation of hematite particles has also been reported at low (< 1.5) and high (> 12) pH due to
301 the elevated ionic strengths[68]. Secondly, our experiments were performed at elevated temperature
302 (35°C) relevant to EARP processes, which gives particles additional thermal energy (kT) to
303 overcome the electrostatic barrier to aggregation. Finally, aggregate formation may be induced
304 by an increase in the concentration of Fe_{13} cluster beyond a certain critical level.
305 The aggregate fractal dimension, d_f increases from ~ 1.1 at pH 1 to ~ 2.3 at pH 3.1 and then
306 stabilizes. A d_f of 1.1 is indicative of highly linear structures[39] and indicates the Fe_{13} clusters are
307 linking into linear aggregates, potentially with some polymerization. This interpretation is
308 supported by the shape of the SAXS patterns between ~ pH 1 and 2, which show an increase in
309 the low-q slope gradient without significant changes to the high-q region (Figure S12). At pH
310 3.1, a d_f of 2.3 indicates more densely packed aggregates with mass fractal structure[39], and
311 therefore shows the aggregates undergo densification with increasing pH, consistent with
312 previous studies which showed densification of iron oxyhydroxide nanoparticles with changing
313 chemical conditions[69,70]. This is concurrent with the rapid decrease in $Fe(III)_{aq}$ and TEM
314 observation of mass fractal aggregates of ~ 3 nm ferrihydrite nanoparticles at pH 3 (Figure S13).

This highlights that during this stage of the reaction (pH up to 3.1) all dissolved $Fe(III)_{aq}$ i.e. Fe_{13} Keggins and smaller hydrolysis products (e.g. monomers and dimers) precipitate to form aggregates of ferrihydrite nanoparticles. We propose that Fe_{13} clusters are preserved within the structure of the ferrihydrite nanoparticles composing these mass fractal aggregates, further details of which are discussed below. Observations show that solutions with pH < 2.0 remain colloidal homogeneous suspensions after > 1 month storage, whilst solutions with pH > 2.0 floc within weeks (Figure S17), consistent with formation of a more densely structured aggregate at increasing pH[40].

The initial fractal dimension of 1.1 is significantly lower than that predicted by traditional models of colloid aggregation. Diffusion limited aggregation (DCA) would be expected to give fractal dimensions of 1.6 – 1.9[71], whilst reaction limited aggregation (RCA) is expected to give fractal dimensions > 2.0[71]. Significantly lower fractal dimensions have previously been reported for iron oxyhydroxide suspensions[39,40] and may possibly be the result of an orientated attachment process whereby aggregation proceeds by preferential attachment at opposite sides of the cluster[39].

Below pH 2, a Guinier region is not observed in the low-q range of the data (Figure 2A and S12), indicating that the aggregates are significantly larger than the maximum size that can be resolved by the experimental q-range (52 nm radius based on the relation, radius = π/q). Correspondingly, the value for ξ (aggregate size parameter) obtained from fitting the scattering patterns between pH 1 and 2 tends to infinity. Above pH 2, the development of curvature in the low-q region (Figure 2A) results in fitting giving considerably smaller values for ξ. This decrease in ξ, concurrent with continually increasing fractal dimension, supports that aggregates undergo collapse to form more compact structures. Following DVLO theory[72], collapse due to pH

increase may be initiated by the decrease in repulsive surface charge, enabling attractive van der Waal forces to dominate. Aggregate densification may further be promoted by condensation of remaining smaller hydrolysis products (e.g. monomers, dimers) with/onto Fe_{13} clusters to form ferrihydrite nanoparticle aggregates. Using Eq.S1 to convert ξ to a radius of gyration (R_g), aggregate R_g subsequently increases from ~ 35 nm at pH 2.3 to ~ 52 nm at pH 4.8. This increase in size is consistent with observation of the low-q Kratky plot peak moving to lower q values (Figure S14A). Above pH 4.8, the aggregates have grown to a size larger than the measured q-range and the R_g value obtained from the model stabilizes. Formation of large aggregates is confirmed by the experiments visibly floccing above pH 4.5 and by TEM images obtained at pH 9 (Figure 4B). Finally, no significant changes occur in the scattering patterns during the 30 min period data continued to be collected at pH 9.

It is noteworthy that the scattering signature from Fe_{13} is seen throughout the experiment (r_0, Figure 2B). This shows structural continuity between isolated Fe_{13} (pH < 1), Fe_{13} aggregates with low fractal dimension (pH 1 – ~ 2), and the ferrihydrite nanoparticle aggregates in which the Fe_{13} motif is preserved (pH > ~ 2). This has also been shown for the Keggin-Al_{13} and $Al(OH)_3$ gel[73,74] system with Al_{13} Keggin units similarly aggregating to form linear clusters with some polymerization, followed by rapid formation of dense, less open clusters[28].

TEM images of the ferrihydrite aggregates at pH 9 (Figure 4B) clearly confirm the expected mass fractal structure from the SAXS analysis. However, higher magnification images show the aggregates are composed of 3 – 4 nm ferrihydrite particles, rather than aggregated Fe_{13} clusters. This may present an apparent inconsistency with the SAXS data which does not account for the ~ 3 – 4 nm ferrihydrite nanoparticles: neither fixing r_0 to 1.5 – 2 nm, nor a two particle model with both Fe_{13} clusters and larger ferrihydrite particles gave acceptable fits. Interestingly, a

surface-depleted model recently proposed by Hiemstra[34,35] indicates that ferrihydrite has a non-homogenous, core-shell structure. We therefore applied fits using the addition of a second structure factor, the hard sphere structure factor, to account for this heterogeneity (Eq S3) (Figure S16). These fits indicate agglomerates with volume fraction $v = 0.09$ composed of particles with hard sphere radius (r_{HS}) 1.47 nm at pH 9, where r_{HS} is calculated based on the mutual spacing between the scatterers (SI). This is consistent with the ~ 3 nm diameter ferrihydrite nanoparticles observed by TEM within aggregates at pH 9 (Figure 4B). Since these hard sphere scatterers are assumed to have the same origin as the ~ 0.45 nm radii clusters seen in the fractal aggregates, this means that the primary scatterers would have an outer, electron-lean shell (depleted in iron and therefore not directly detected by SAXS measurements) of thickness $r_{HS} - r_0 \sim 1$ nm. Hiemstra's surface-depleted ferrihydrite model consists of a defect-free core and a water-rich surface layer which is depleted in the Fe2 and Fe3 polyhedra of the Michel model[32]. This model is also supported by Wang *et al.*[62], whose results indicate that 1.6 nm ferrihydrite particles have an amorphous surface layer which accounts for ~38 % of their total volume, corresponding to a core size of 1.36 nm and surface layer thickness of 0.12 nm. Interestingly, this surface layer thickness is smaller than those calculated for our systems but we note the published work was based on a dried sample, whilst our work is based on *in situ* analysis of particle suspended in aqueous solution. Fits obtained with the addition of the hard sphere structure factor are improved compared to regular model fits at pH > 3 (Figure S16 and Table S3), whilst < pH 2.25 fits give a value of 0 for v, indicating no contribution from this structure factor (Table S3). This is also the critical pH range (pH 2 – 3) where ferrihydrite nanoparticle formation/aggregation occurs (Figure 1 and 2B). Further, pH 2 – 3 is when $Fe(III)_{aq}$ decreases rapidly (Figure 1) which may be related to the condensation of smaller hydrolysis products (e.g. monomers and dimers)

onto Fe_{13} cluster leading to the development of the core-shell structure whereby surface bound OH and OH_2 are retained, resulting in a water-rich/Fe-depleted surface layer on a Keggin cluster core in line with the Hiemstra model[34]. We propose this is the dominant pathway of ferrihydrite formation in our system. An alternative pathway via direct nucleation of ferrihydrite particles from small hydrolysis products (monomers, dimers), without the involvement of Fe_{13}, can be ruled out because the SAXS data shows no evidence for direct formation of > 2 nm particles. Overall, inclusion of the hard spheres structure factor suggests the formation of ~ 3 nm ferrihydrite particles with a core-shell structure composed of a Fe_{13} core (which is what the SAXS directly "sees") and a Fe depleted shell.

Implications for ferrihydrite formation. We provide the first direct *in situ* observations of Fe_{13} Keggin prenucleation cluster formation during hydrolysis of a ferric iron solution followed by the formation of aggregated ferrihydrite nanoparticles. The ferrihydrite formation process mimicked the EARP industrial process and involved continual addition of a strong base (7 M) to a highly acidic ferric nitrate solution (1 M HNO_3). Such extremes in pH have rarely been examined with most studies conducted on quasi-equilibrated solutions between pH 1 and 4. In our systems, Fe_{13} clusters may form rapidly within localized areas of high pH via the well described successive polymerization Fe hydrolysis steps[13], and interestingly, their formation seems to be essentially irreversible with the Keggin apparently stabilized against aggregation at pH < ~ 1, probably due to the high charge on the clusters. This localized formation model is supported by the absence of Fe_{13} clusters in pH 1 ferric nitrate solution which was prepared by directly dissolving $Fe(NO_3)_3$ in 0.1 M HNO_3 (Figure S15). This sensitivity to the preparation method has been found for Al salts[26], with formation of the Al_{13} cluster coinciding with strong base neutralization of Al salt solutions[26,27]. It is thought that the tetrahedral $Al(OH)_4^-$ ion, formed

in the locally high pH region at the point of base injection, is required for Al_{13} synthesis[75,76]. An analogous $Fe(OH)_4^-$ ion exists[25,77] and may similarly promote Fe_{13} cluster formation. Dependence on solution conditions and experimental protocol may explain why Fe_{13} was not detected in recent XAS studies[14–16]. These used non-acidified ferric solutions that were neutralized with weak bases, concluding that an μ-oxo Fe(III) dimer was the dominant species present. Additionally, EXAFS analysis gives the average local environment of all Fe within a system, therefore if Fe_{13} clusters were present at low proportions (< 10 – 20 %) this may not be detected by XAS. In contrast, SAXS analysis preferentially detects larger clusters/particles, but not smaller molecules (e.g. monomers). However, recent SAXS studies performed at constant pH 3.7[78] and pH 3[12] reported rapid formation of 3 nm iron oxyhydroxide nanoparticles which subsequently grew to 7-10 nm. No smaller clusters were reported, highlighting that Fe_{13} is either highly transitory or not formed under these higher pH conditions.

In the systems studied, Fe_{13} clusters were stable in pH 0.5 and 1.5 solution for at least 18 days (Figure S8). Al_{13} is also stable in aqueous solutions for long periods (> 12 years) over a wide pH range[29,64,65]. Sadeghi *et al.*[31] used Bi^{3+} ions to stabilize Fe_{13} in solution, whereby the Bi^{3+} acts to neutralize high negative cluster charge. Stability in the present study may be promoted by the elevated ionic strength of the solution, with H^+ and Na^+ ions acting as inherent stabilizing ions. Indeed, Sadeghi *et al.*[31] found Cs^+ could partially displace Bi^{3+} and maintain the discrete Fe_{13} units (albeit with a small amount of aggregation), consistent with monovalent ions being able to stabilise these clusters.

Environmental Significance. Given the apparent dependence of Fe_{13} formation on solution conditions, it is unclear whether the ferrihydrite formation pathway observed in the present study also occurs in the natural environment. A similar debate has taken place about the Al

system[64,75,79]. Furrer *et al.*[80] reported that Al flocs, which were generated by the mixing of acidic mining streams with higher pH water, comprised of aggregated Al_{13} clusters. Our study indicates that Fe_{13} is only stable at pH < ~ 1, above which it rapidly aggregates. In the natural environment ferrihydrite often forms by oxidation of $Fe(II)_{aq}$ at near neutral pH[1] and under these conditions Fe_{13}, if formed, would be expected to be highly transitory. In acidic conditions, such as in acid mine runoff, Fe_{13} may be more persistent. Indeed, Zhu *et al.*[67] reported formation of "ferrihydrite-like" molecular clusters during neutralization of simulated acid mine drainage solutions, speculating that these clusters may resemble the Fe_{13} motif. Additionally, Sadeghi *et al.*[31] note that complexing ligands similar to the TCA ligand utilized to stabilize the cluster in their work have parallel models in nature (e.g. carboxylic groups) which may act to stabilize the clusters. Ultimately, further work is required to investigate the importance of an Fe_{13} pathway to ferrihydrite formation in the natural environment.

FIGURES

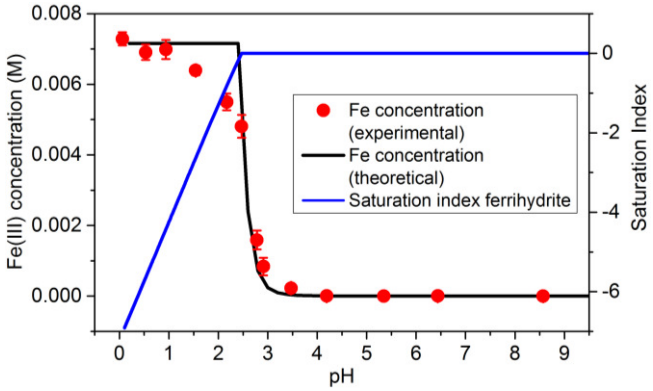

Figure 1. $Fe(III)_{aq}$ concentration with pH for the standard NaOH addition experiment, with simulated concentration and saturation index for ferrihydrite obtained using PHREEQC. Both the experimental and theoretical Fe concentrations are corrected for dilution caused by NaOH addition. Error bars show ± one standard deviation based on three repeat measurements.

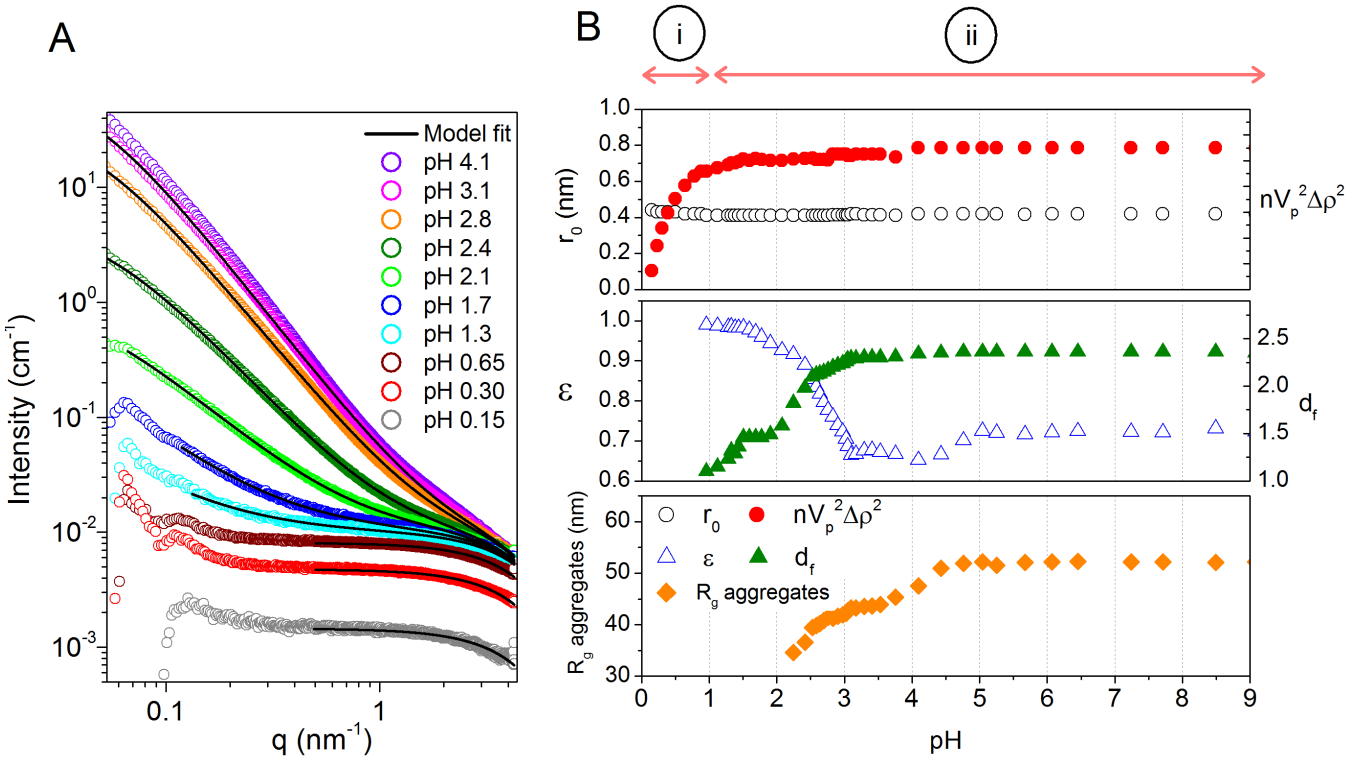

Figure 2. A) A selection of time-resolved *in situ* SAXS patterns collected during ferrihydrite formation (standard NaOH addition rate) with model fits overlain. B) Evolution of particle radius (r_0), pre-factor term ($nV_p^2\Delta\rho^2$), aggregate weighting factor (ε), aggregate fractal dimension (d_f) and aggregate radius of gyration (R_g aggregates) during ferrihydrite formation (standard NaOH addition rate). The start of stages i and ii of the reaction are marked (see main text).

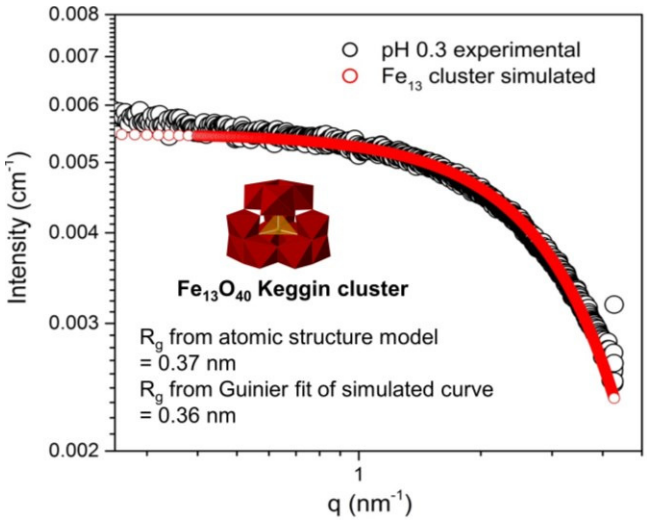

Figure 3. Simulated scattering curve for a Fe_{13} Keggin cluster compared to the experimental scattering curve collected at pH 0.3. Inset is an atomic structure model of a Fe_{13} cluster[31] with radii of gyration (Rg) calculated by Crysol based on both the atomic structure model and the Guinier fit of the simulated curve.

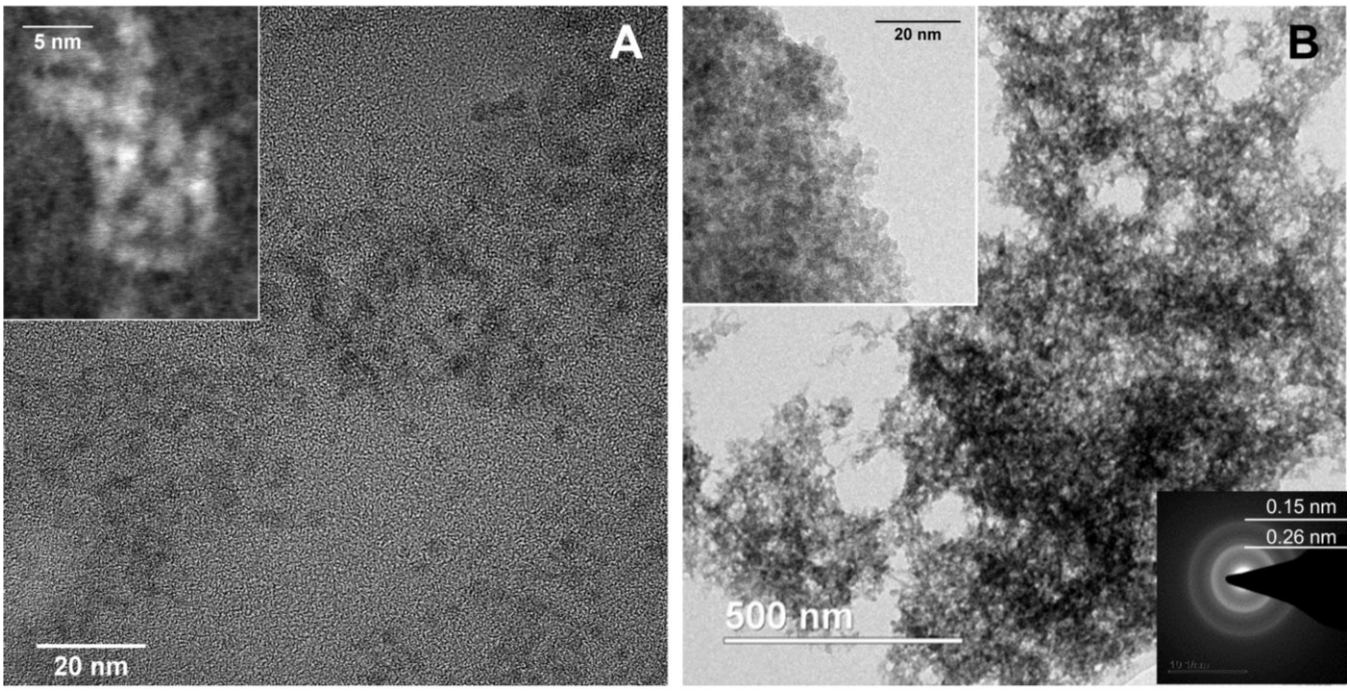

Figure 4. A) TEM images of particles from pH 1 experimental solution showing aggregates of 2-5 nm sized ferrihydrite particles. Inset high angle angular dark field (HAADF) image of an aggregate. B) TEM images of particles from pH 9 experimental solution showing ferrihydrite aggregates with mass fractal structure. Top left inset showing individual particle sizes of 3-4 nm. Bottom right inset electron diffraction pattern inset showing characteristic 2-line ferrihydrite diffraction.

ASSOCIATED CONTENT

Supporting Information

Further experimental details of SAXS analysis, TEM image collection, ultrafiltration experiments and PHREEQC modelling. XRD pattern, aged sample SAXS patterns, time lapse video of reaction progress, and further solution data, SAXS figures and TEM images. This material is available free of charge via the Internet at http://pubs.acs.org.

AUTHOR INFORMATION

Corresponding Author

Email: sam.shaw@manchester.ac.uk

Tel: 0161 275-3826

Address: Williamson Building, School of Earth, Atmospheric and Environmental Sciences, The University of Manchester, Manchester, M13 9PL

Present Addresses

† Department of Civil and Environmental Engineering, University of Strathclyde, Glasgow G1 1XJ, UK

Author Contributions

The manuscript was written through contributions of all authors. All authors have given approval to the final version of the manuscript.

Funding Sources

Sellafield Ltd and The University of Manchester co-funded this work via the Effluents and Decontamination Centre of Excellence. This work was also supported by Environmental Radioactivity Research Network (grant number ST/K001787/1).

ACKNOWLEDGMENT

Sellafield Ltd and The University of Manchester co-funded this work via the Effluents and Decontamination Centre of Excellence. This work was also supported by Environmental

Radioactivity Research Network (grant number ST/K001787/1). Diamond Light Source provided beamtime awards (SM12704 and SM11075) and we thank Andy Smith and Nick Terrill for beamline assistance. We also thank Ellen Winstanley, Andy Brown and Graham Kenyon for assistance during analyses.

REFERENCES

(1) Cornell, R. M.; Schwertmann, U. *The Iron Oxides: Structure, Properties, Reactions, Occurances and Uses*; Wiley-VCH: Wienheim, 2003.

(2) Violante, A.; Gaudio, S. D.; Pigna, M.; Ricciardella, M.; Banerjee, D. Coprecipitation of arsenate with metal oxides. 2. Nature, mineralogy, and reactivity of iron (III) precipitates. *Environ. Sci. Technol.* **2007**, *41* (24), 8275–8280.

(3) Kinniburgh, D. G.; Jackson, M. L.; Syers, J. K. Adsorption of Alkaline Earth, Transition, and Heavy Metal Cations by Hydrous Oxide Gels of Iron and Aluminum. *Soil Sci. Soc. Am. J.* **1976**, *40* (5), 796–799.

(4) Ping, L.; Zhuoxin, Y.; Jianfeng, L.; Qiang, J.; Yaofang, D.; Qiaohui, F.; Wangsuo, W. The immobilization of U(VI) on iron oxyhydroxides under various physicochemical conditions. *Environ. Sci. Proceeses Impacts* **2014**, *16*, 2278–2287.

(5) Xu, P.; Zeng, G. M.; Huang, D. L.; Feng, C. L.; Hu, S.; Zhao, M. H.; Lai, C.; Wei, Z.; Huang, C.; Xie, G. X.; et al. Use of iron oxide nanomaterials in wastewater treatment: A review. *Sci. Total Environ.* **2012**, *424*, 1–10.

(6) Fu, D.; Keech, P. G.; Sun, X.; Wren, J. C. Iron oxyhydroxide nanoparticles formed by

forced hydrolysis: dependence of phase composition on solution concentration. *Phys. Chem. Chem. Phys.* **2011**, *13* (41), 18523.

(7) Liu, H.; Li, X.; Wang, Y.; Yang, X.; Zhen, Z.; Chen, R.; Hou, D.; Wei, Y. New insight into the effect of the formation environment of ferrihydrite on its structure and properties. *RSC Adv.* **2014**, *4* (22), 11451.

(8) Spiro, T.; Allerton, S.; Renner, J.; Aristides, T.; Bils, R.; Saltman, P. The hydrolytic polymerization of iron (III). *J. Am. Chem. Soc.* **1966**, *1* (5), 2721–2726.

(9) Knight, R. J.; Sylva, R. N. Precipitation in hydrolysed iron(III) solutions. *J. Inorg. Nucl. Chem.* **1974**, *36* (3), 591–597.

(10) Flynn Jr., C. M. Hydrolysis of inorganic iron(III) salts. *Chem. Rev.* **1984**, *84* (1), 31–41.

(11) Schwertmann, U.; Friedl, J.; Stanjek, H. From Fe(III) Ions to Ferrihydrite and then to Hematite. *J. Colloid Interface Sci.* **1999**, *209* (1), 215–223.

(12) Rose, A. L.; Bligh, M. W.; Collins, R. N.; Waite, T. D. Resolving early stages of homogeneous iron(III) oxyhydroxide formation from iron(III) nitrate solutions at pH 3 using time-resolved SAXS. *Langmuir* **2014**, *30* (12), 3548–3556.

(13) Jolivet, J. P.; Chanéac, C.; Tronc, E. Iron oxide chemistry. From molecular clusters to extended solid networks. *Chem. Commun.* **2004**, *5*, 481–487.

(14) Zhu, M.; Puls, B. W.; Frandsen, C.; Kubicki, J. D.; Zhang, H.; Waychunas, G. A. In situ structural characterization of ferric iron dimers in aqueous solutions: Identification of μ-oxo species. *Inorg. Chem.* **2013**, *52*, 6788–6797.

(15) Zhu, M.; Frandsen, C.; Wallace, A. F.; Legg, B.; Khalid, S.; Zhang, H.; Mørup, S.; Banfield, J. F.; Waychunas, G. A. Precipitation Pathways for Ferrihydrite Formation in Acidic Solutions. *Geochim. Cosmochim. Acta* **2016**, *172* (1), 247–264.

(16) Collins, R. N.; Rosso, K. M.; Rose, A. L.; Glover, C. J.; Waite, T. D. An in situ XAS study of ferric iron hydrolysis and precipitation in the presence of perchlorate, nitrate, chloride and sulfate. *Geochim. Cosmochim. Acta* **2016**, *177*, 150–169.

(17) Johnston, J. H.; Lewis, D. G. A Study of the Initially-Formed Hydrolysis Species and Intermediate Polymers and their Role in Determining the Product Iron Oxides Formed in the Weathering of Iron. In *Industrial Applications of the Mossbauer Effect*; Long, G. L., Stevens, J. G., Eds.; Plenum Press: New York, 1986; pp 565–683.

(18) Lopes, L.; De Laat, J.; Legube, B. Charge transfer of iron(III) monomeric and oligomeric aqua hydroxo complexes: Semiempirical investigation into photoactivity. *Inorg. Chem.* **2002**, *41* (9), 2505–2517.

(19) Vilgé-Ritter, A.; Rose, J.; Masion, A.; Bottero, J.-Y.; Lainé, J.-M. Chemistry and structure of aggregates formed with Fe-salts and natural organic matter. *Colloids Surfaces A Physicochem. Eng. Asp.* **1999**, *147* (3), 297–308.

(20) Melikhov, I. V; Kozlovskaya, E. D.; Berliner, L. B.; Prokofiev, M. A. Kinetics of hydroxide Fe(III) solid phase formation. *J. Colloid Interface Sci.* **1987**, *117* (1), 1–9.

(21) Rose, J.; Manceau, A.; Masion, A.; Bottero, J. Y. Structure and mechanisms of formation of FeOOH(NO3) oligomers in the early stages of hydrolysis. *Langmuir* **1997**, *13* (12), 3240–3246.

(22) Bradley, S. M.; Lehr, C. R.; Kydd, R. A. Base hydrolysis of aqueous chromium(III) solutions: on the existence of [Cr(OH)4], and speculation regarding a new chromium polyoxocation. *J. Chem. Soc. Dalt. Trans.* **1993**, *15*, 2415.

(23) Torapava, N.; Radkevich, A.; Davydov, D.; Titov, A.; Persson, I. Composition and structure of polynuclear chromium(III) hydroxo complexes. *Inorg. Chem.* **2009**, *48* (21), 10383–10388.

(24) Michot, L. J.; Montargès-Pelletier, E.; Lartiges, B. S.; D'Espinose De La Caillerie, J. B.; Briois, V. Formation mechanism of the Ga13 Keggin ion: A combined EXAFS and NMR study. *J. Am. Chem. Soc.* **2000**, *122* (26), 6048–6056.

(25) Bradley, S. M.; Kydd, R. A. Comparison of the species formed upon base hydrolyses of gallium(III) and iron(III) aqueous solutions: the possibility of existence of an [FeO4Fe12(OH)24(H2O)12]7+ polyoxocation. *J. Chem. Soc. Dalt. Trans.* **1993**, *15*, 2407.

(26) Akitt, J. W.; Greenwood, N. N.; Khandelwal, B. L.; Lester, G. D. 27 Al nuclear magnetic resonance studies of the hydrolysis and polymerisation of the hexa-aquo-aluminium(III) cation. *J. Chem. Soc. Dalt. Trans.* **1971**, *5*, 604–610.

(27) Parker, D. R.; Bertsch, P. M. Identification and quantification of the "Al13" tridecameric aluminum polycation using ferron. *Environ. Sci. Technol.* **1992**, *26* (5), 908–914.

(28) Bottero, J. Y.; Axelos, M.; Tchoubar, D.; Cases, J. M.; Fripiat, J. J.; Fiessinger, F. Mechanism of formation of aluminum trihydroxide from keggin Al13 polymers. *J. Colloid Interface Sci.* **1987**, *117* (1), 47–57.

(29) Casey, W. H. Large aqueous aluminum hydroxide molecules. *Chem. Rev.* **2006**, *106* (1),

641 1–16.

642 (30) Armstrong, C. R.; Casey, W. H.; Navrotsky, A. Energetics of Al13 Keggin cluster
643 compounds. *Proc. Natl. Acad. Sci. U. S. A.* **2011**, *108* (36), 14775–14779.

644 (31) Sadeghi, O.; Zakharov, L. N.; Nyman, M. Aqueous formation and manipulation of the
645 iron-oxo Keggin ion. *Science* **2015**, *347* (6228), 1359–1362.

646 (32) Michel, F. M.; Ehm, L.; Antao, S. M.; Lee, P. L.; Chupas, P. J.; Liu, G.; Strongin, D. R.;
647 Schoonen, M. A. A.; Phillips, B. L.; Parise, J. B. The structure of ferrihydrite, a
648 nanocrystalline material. *Science* **2007**, *316* (5832), 1726–1729.

649 (33) Maillot, F.; Morin, G.; Wang, Y.; Bonnin, D.; Ildefonse, P.; Chaneac, C.; Calas, G. New
650 insight into the structure of nanocrystalline ferrihydrite: EXAFS evidence for tetrahedrally
651 coordinated iron(III). *Geochim. Cosmochim. Acta* **2011**, *75* (10), 2708–2720.

652 (34) Hiemstra, T. Surface and mineral structure of ferrihydrite. *Geochim. Cosmochim. Acta*
653 **2013**, *105*, 316–325.

654 (35) Hiemstra, T. Formation, stability, and solubility of metal oxide nanoparticles: Surface
655 entropy, enthalpy, and free energy of ferrihydrite. *Geochim. Cosmochim. Acta* **2015**, *158*,
656 179–198.

657 (36) Peak, D.; Regier, T. Direct observation of tetrahedrally coordinated Fe(III) in ferrihydrite.
658 *Environ. Sci. Technol.* **2012**, *46* (6), 3163–3168.

659 (37) Gebauer, D.; Kellermeier, M.; Gale, J. D.; Bergström, L.; Cölfen, H. Pre-nucleation
660 clusters as solute precursors in crystallisation. *Chem. Soc. Rev.* **2014**, *43* (7), 2348–2371.

(38) Yuwono, V. M.; Burrows, N. D.; Soltis, J. A.; Anh Do, T.; Lee Penn, R. Aggregation of ferrihydrite nanoparticles in aqueous systems. *Faraday Discuss.* **2012**, *159*, 235.

(39) Legg, B. A.; Zhu, M.; Comolli, L. R.; Gilbert, B.; Banfield, J. F. Determination of the three-dimensional structure of ferrihydrite nanoparticle aggregates. *Langmuir* **2014**, *30* (33), 9931–9940.

(40) Legg, B. A.; Zhu, M.; Comolli, L. R.; Gilbert, B.; Banfield, J. F. Impacts of ionic strength on three-dimensional nanoparticle aggregate structure and consequences for environmental transport and deposition. *Env. Sci Technol* **2014**, *48* (23), 13703–13710.

(41) Gilbert, B.; Lu, G.; Kim, C. S. Stable cluster formation in aqueous suspensions of iron oxyhydroxide nanoparticles. *J. Colloid Interface Sci.* **2007**, *313* (1), 152–159.

(42) Dale, J. G.; Stegemeier, J. P.; Kim, C. S. Aggregation of nanoscale iron oxyhydroxides and corresponding effects on metal uptake, retention, and speciation: I. Ionic-strength and pH. *Geochim. Cosmochim. Acta* **2015**, *148*, 100–112.

(43) Stegemeier, J. P.; Reinsch, B. C.; Lentini, C. J.; Dale, J. G.; Kim, C. S. Aggregation of nanoscale iron oxyhydroxides and corresponding effects on metal uptake, retention, and speciation: II. Temperature and time. *Geochim. Cosmochim. Acta* **2015**, *148*, 113–129.

(44) Gilbert, B.; Ono, R. K.; Ching, K. A.; Kim, C. S. The effects of nanoparticle aggregation processes on aggregate structure and metal uptake. *J. Colloid Interface Sci.* **2009**, *339* (2), 285–295.

(45) Loan, M.; Parkinson, G.; Newman, M.; Farrow, J. Iron oxy-hydroxide crystallization in a hydrometallurgical residue. *J. Cryst. Growth* **2002**, *235* (1-4), 482–488.

682 (46) Baumgartner, J.; Faivre, D. Iron solubility, colloids and their impact on iron
683 (oxyhydr)oxide formation from solution. *Earth-Science Rev.* **2015**, *150*, 520–530.

684 (47) Hutson, G. V. Waste Treatment. In *The Nuclear Fuel Cycle: from Ore to Wastes*; Wilson,
685 P. D., Ed.; Oxford University Press: Oxford, 1996; pp 161–183.

686 (48) Hildred, K. L.; Townson, P. S.; Hutson, G. V.; Williams, R. A. Characterisation of
687 particulates in the BNFL Enhanced Actinide Removal Plant. *Powder Technol.* **2000**, *108*
688 (2-3), 164–172.

689 (49) Viollier, E.; Inglett, P. W.; Hunter, K.; Roychoudhury, A. N.; Van Cappellen, P. The
690 ferrozine method revisited: Fe(II)/Fe(III) determination in natural waters. *Appl.*
691 *Geochemistry* **2000**, *15* (6), 785–790.

692 (50) Parkhurst, D. L.; Appelo, C. A. J. Description of Input and Examples for PHREEQC
693 Version 3 — A Computer Program for Speciation , Batch-Reaction , One-Dimensional
694 Transport , and Inverse Geochemical Calculations Chapter 43 of. In *Modeling Techniques,*
695 *Book 6*; USGS: Denver, 2013; pp 1–678.

696 (51) Ahmed, I. A. M.; Benning, L. G.; Kakonyi, G.; Sumoondur, A. D.; Terrill, N. J.; Shaw, S.
697 Formation of green rust sulfate: A combined in situ time-resolved X-ray scattering and
698 electrochemical study. *Langmuir* **2010**, *26* (9), 6593–6603.

699 (52) Stawski, T. M.; Veldhuis, S. A.; Besselink, R.; Castricum, H. L.; Portale, G.; Blank, D. H.
700 A.; Elshof, J. E. Nanoscale Structure Evolution in Alkoxide-Carboxylate Sol-Gel
701 Precursor Solutions of Barium Titanate. *J. Phys. Chem. C* **2011**, *115*, 20449–20459.

702 (53) Jambor, J. L.; Dutrizac, J. E. Occurrence and Constitution of Natural and Synthetic

Ferrihydrite, a Widespread Iron Oxyhydroxide. *Chem. Rev.* **1998**, *98* (7), 2549–2586.

(54) Guinier, A.; Fourner, G. Small-Angle Scattering of X-rays. In *Small-Angle Scattering of X-rays*; Wiley: New York, 1955.

(55) Pauw, B. R. Everything SAXS: small-angle scattering pattern collection and correction. *J. Phys. Condens. Matter* **2013**, *25* (38), 383201.

(56) Baes, C.; Mesmer, R. *The hydrolysis of cations*; Krieger Pub Co, 1976.

(57) Dousma, J.; de Bruyn, P. L. Hydrolysis-precipitation studies of iron solutions. I. Model for hydrolysis and precipitation from Fe(III) nitrate solutions. *J. Colloid Interface Sci.* **1976**, *56* (3), 527–539.

(58) Dousma, J.; De Bruyn, P. L. Hydrolysis—precipitation studies of iron solutions. II. Aging studies and the model for precipitation from Fe(III) nitrate solutions. *J. Colloid Interface Sci.* **1978**, *64* (1), 154–170.

(59) Van Der Woude, J. H. A.; Verhees, P.; De Bruyn, P. L. Formation of colloidal dispersions from supersaturated iron(III) nitrate solutions. II. Kinetics of growth at elevated temperatures. *Colloids and Surfaces* **1983**, *8* (1), 79–92.

(60) Masion, A.; Rose, J.; Bottero, J.-Y.; Tchoubar, D.; Elmerich, P. Nucleation and Growth Mechanisms of Iron Oxyhydroxides in the Presence of PO_4 Ions . 3. Speciation of Fe by Small Angle X-ray Scattering. *Langmuir* **1997**, *13* (19), 3882–3885.

(61) Janney, D. E.; Cowley, J. M.; Buseck, P. R. Transmission Electron Microscopy of Synthetic 2- and 6-Line Ferrihydrite. *Clays Clay Miner.* **2000**, *48* (1), 111–119.

(62) Wang, X.; Zhu, M.; Koopal, L. K.; Li, W.; Xu, W.; Liu, F.; Zhang, J.; Qingsong, L.; Feng, X.; Sparks, D. L. Effects of crystallite size on the structure and magnetism of ferrihydrite. *Environ. Sci. Nano* **2016**, *3*, 190–202.

(63) Wang, D.; Wang, S.; Huang, C.; Chow, C. W. K. Hydrolyzed Al(III) clusters: Speciation stability of nano-Al13. *J. Environ. Sci.* **2011**, *23* (5), 705–710.

(64) Etou, A.; Bai, S.; Saito, T.; Noma, H.; Okaue, Y.; Yokoyama, T. Formation conditions and stability of a toxic tridecameric Al polymer under a soil environment. *J. Colloid Interface Sci.* **2009**, *337* (2), 606–609.

(65) Duan, J.; Gregory, J. Coagulation by hydrolysing metal salts. *Adv. Colloid Interface Sci.* **2003**, *100-102*, 475–502.

(66) Kato, C. N.; Katayama, Y.; Nagami, M.; Kato, M.; Yamasaki, M. A sandwich-type aluminium complex composed of tri-lacunary Keggin-type polyoxotungstate: synthesis and X-ray crystal structure of [(A-PW9O34)2{W(OH)(OH2)}{Al(OH)(OH2)}{Al(μ-OH)(OH2)2}2]7−. *Dalt. Trans.* **2010**, *39*, 11469–11474.

(67) Zhu, M.; Legg, B.; Zhang, H.; Gilbert, B.; Ren, Y.; Banfield, J. F.; Waychunas, G. A. Early stage formation of iron oxyhydroxides during neutralization of simulated acid mine drainage solutions. *Environ. Sci. Technol.* **2012**, *46* (15), 8140–8147.

(68) Matijevic, E. Colloid chemical aspects of corrosion of metals. *Pure Appl. Chem.* **1980**, *52* (5), 1179–1193.

(69) Bottero, J. Y.; Tchoubar, D.; Arnaud, M.; Quienne, P. Partial hydrolysis of ferric nitrate salt - structural investigation by dynamic light-scattering and small-angle x- ray-

scattering. *Langmuir* **1991**, *7* (7), 1365–1369.

(70) Tchoubar, D.; Bottero, J. Y.; Quienne, P.; Arnaud, M. Partial hydrolysis of ferric-chloride salt - structural investigation by photon-correlation spectroscopy and small- angle x-ray-scattering. *Langmuir* **1991**, *7* (2), 398–402.

(71) Sposito, G. Scaling invariance of the von Smoluchowski rate law. *Colloids Surf., A* **1997**, *120*, 101–110.

(72) Elimelech, M.; Gregory, J.; Jia, X.; Williams, R. *Particle Deposition & Aggregation: Measurement, Modelling and Simulation*, 1st ed.; Butterworth-Heinemann Ltd: Oxford, 1995.

(73) Bottero, J. Y.; Tchoubar, D.; Cases, J. M.; Flessinger, F. Investigation of the Hydrolysis of Aqueous Solutions of Aluminum Chloride. 2. Nature and Structure by Small-Angle X-ray Scattering. *J. Phys. Chem.* **1982**, *86*, 3667–3673.

(74) Bi, Z.; Chen, Y.; Wang, S.; Wang, D. Hydrolyzed Al(III)-clusters. II: Speciation transformation and stability of Al13 aggregates. *Colloids Surfaces A Physicochem. Eng. Asp.* **2014**, *440*, 59–62.

(75) Bertsch, P. M. Conditions for Al13 Polymer Formation in Partially Neutralised Aluminium Solutions. *Soil Sci. Soc. Am. J.* **1986**, *51* (3), 825–828.

(76) Kloprogge, J. T.; Seykens, D.; Jansen, J. B. H.; Geus, J. W. A 27Al nuclear magnetic resonance study on the optimalization of the development of the Al13 polymer. *J. Non. Cryst. Solids* **1992**, *142*, 94–102.

(77) Diakonov, I. I.; Schott, J.; Martin, F.; Harrichourry, J. C.; Escalier, J. Iron(III) solubility

765 and speciation in aqueous solutions. Experimental study and modelling: Part 1. Hematite
766 solubility from 60 to 300??C in NaOH-NaCl solutions and thermodynamic properties of
767 Fe(OH)4-(aq). *Geochim. Cosmochim. Acta* **1999**, *63* (15), 2247–2261.

768 (78) Hu, Y.; Lee, B.; Bell, C.; Jun, Y. S. Environmentally abundant anions influence the
769 nucleation, growth, ostwald ripening, and aggregation of hydrous Fe(III) oxides.
770 *Langmuir* **2012**, *28* (20), 7737–7746.

771 (79) Hunter, D.; Ross, D. S. Evidence for a phytotoxic hydroxy-aluminum polymer in organic
772 soil horizons. *Science* **1991**, *251* (4997), 1056–1058.

773 (80) Furrer, G.; Phillips, B. L.; Ulrich, K. U.; Pöthig, R.; Casey, W. H. The origin of aluminum
774 flocs in polluted streams. *Science* **2002**, *297* (5590), 2245–2247.

775

776

777 TABLE OF CONTENTS (TOC) ART

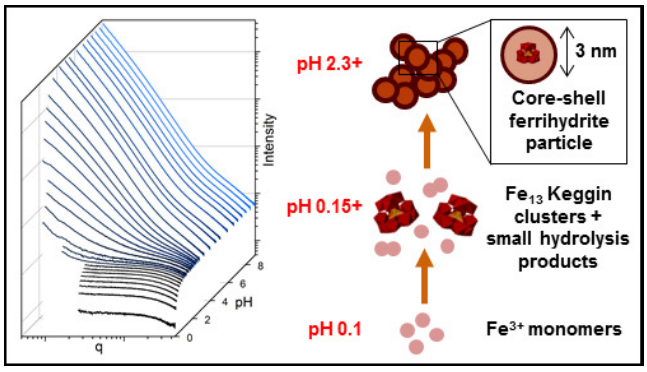

778

779